Digital Object Identifier 10.1109/TPEL.2018.2848109

A Novel AC Power Loss Model for Ferrite Power Inductors

Kateryna Stoyka, Giulia Di Capua, *Member, IEEE*, and Nicola Femia, *Senior Member, IEEE*

***Abstract*—Recent studies have proved that sustainable saturation operation of Ferrite Power Inductors (FPIs) allows reducing the inductor size and increasing the power density in Switch-Mode Power Supply (SMPS) applications. This paper discusses a new behavioral model for reliable prediction of *ac* power loss in FPIs, including the effects of saturation. The new model has been identified by means of the Genetic Programming (GP) algorithm combined with a Multi-Objective Optimization (MOO) technique, starting from large sets of power loss experimental measurements. The proposed *ac* power loss model uses as input variables the voltage and switching frequency imposed to the inductor by the SMPS operation, while the *dc* inductor current is used as a parameter expressing the impact of saturation. Such quantities can be easily determined for whatever converter topology and in real-world switching operation, thus confirming the readiness and the easiness-to-use of the proposed behavioral model. The results of experimental tests presented in this paper prove the reliability of the power loss predictions, also by correctly accounting for the impact of inductors saturation.**

***Index Terms*—Ferrite Power Inductors, Genetic Programming, Multi-Objective Optimization, Modeling, Power Loss, Saturation.**

ABBREVIATIONS

FPI	Ferrite Power Inductor.
SMPS	Switch-Mode Power Supply.
GP	Genetic Programming.
MOO	Multi-Objective Optimization.
SE	Steinmetz Equation.
i-GSE	*improved* Generalized Steinmetz Equation.
NLLS	Non-Linear Least Squares.
RMSE	Root Mean Square Error.

I. INTRODUCTION

SATURATION represents an important characteristic of all magnetic components. In power inductors, such nonlinear phenomenon yields a progressive inductance decrease while the average inductor current increases [1]. Ferrite Power Inductors (FPIs) are conventionally adopted in Switch-Mode Power Supply (SMPS) design when high efficiency and high power density are required. FPIs exhibit a rapid transition to saturation when the current exceeds a certain threshold. In SMPS design, it is commonly considered a good practice to select FPIs operating in the region of weak saturation (within about 20% inductance drop) [2]. Nevertheless, saturation is not a real issue, neither for the inductor nor for the entire converter, if the current ripple, the power loss and the temperature rise fall within limits suitable both for the device and for the application [3]. Recent studies have highlighted that the sustainable saturation operation of FPIs allows to achieve a reduction of the inductor size and an increase of the SMPS power density [1], [3]–[6]. However, appropriate saturation models and power loss models are needed for reliable current ripple and power loss prediction in partial saturation conditions.

The FPIs power loss is determined by magnetic core loss and winding loss, which depend on:

1) *core volume and geometry*, characterized by sharp edges and not allowing easy analytical modeling;
2) *core materials*, whose characteristics are not disclosed by inductors manufacturers;
3) *winding arrangement*, where skin and proximity effects can occur since Litz wires are not usually adopted for commercial parts.

However, the core and winding losses cannot be easily measured as separate contributions in SMPS applications. FPIs power loss can also be evaluated as the sum of a *dc* term and an *ac* term. The *dc* loss is only due to the *dc* current flowing through the winding. The *ac* loss includes the contributions of both winding and magnetic core. Since the *dc* loss can be easily estimated from the *dc* winding resistance, the major challenge still remains how to determine the total *ac* loss in FPIs.

This paper discusses a new behavioral *ac* loss model for FPIs in SMPS applications, including the effects of saturation. The model uses as input variables the voltage and switching frequency imposed to the inductor by the SMPS operation, while the *dc* inductor current is used as a parameter expressing the impact of saturation. The proposed model has been generated by means of a Genetic Programming (GP) algorithm combined with a Multi-Objective Optimization (MOO) technique. The GP algorithm is often used in scientific investigations aimed at generating behavioral models of systems and devices, whose physical behavior is unknown or too complicated to describe with physical laws [7]. The GP approach allows to identify both the model structure and relevant parameters, given a set of

This work was supported by the University of Salerno through the project "*Modellistica e Applicazioni di Induttori di Potenza in Saturazione*" (300638FRB16FEMIA).

The authors are with the Department of Information and Electrical Engineering and Applied Mathematics, University of Salerno, Fisciano 84084, Italy (e-mail: kstoyka@unisa.it; gdicapua@unisa.it; femia@unisa.it).

experimental data and the list of variables adopted in the model. In this paper, the GP-MOO approach has been adopted to identify the *ac* loss model of FPIs ensuring an optimal trade-off between accuracy and complexity.

The paper is organized as follows. In Section II, a brief State-of-the-Art on inductors power loss modeling is provided. In Section III, the main elements of the GP-MOO approach adopted for the identification of the FPIs *ac* loss models are illustrated. In Section IV, the *ac* loss model generated by using the GP-MOO approach is presented, and its reliability and accuracy are discussed and confirmed by comparison with experimental results. In Appendix A, the coefficients determination for classical FPIs core loss models is comprehensively discussed. In Appendix B, details about the GP-MOO approach are eventually provided.

II. Inductor Power Loss

Several literature contributions have been presented on high-frequency loss measurement techniques for magnetic components [8]–[14]. In the classical four-wire two-winding method, the core under test is wound as a transformer [8][9]: excitation is inserted on the core through one winding, and voltage is measured on the other sensing winding. The core loss is then evaluated by integrating the product of the voltage on sensing winding and the current through the excitation winding. A third winding can be possibly considered to test a given *dc* premagnetization condition [10]. The two-winding methods have no significant drawbacks in principle. They allow to measure the core loss and exclude the winding loss, but are sensitive to phase discrepancy mainly due to current sensing, probe mismatch and oscilloscope time resolution limit. New compensation methods consider capacitive cancellation for core loss measurement at very high frequencies [11][12]. A capacitor is connected in series with the inductor of the core under test and finely tuned to resonate with it at the test frequency. The core loss can be measured after compensating the parasitic resistances. These compensation methods automatically exclude the loss of the excitation winding and greatly reduce the sensitivity to phase discrepancy. However, in certain conditions, it could be difficult to realize an exact compensation at the excitation frequency: the value of the cancellation capacitor is quite critical, and a small variation can induce a big measurement error [13]. Finally, enhanced compensation methods rely on an inductive cancellation approach [14], to further reduce the phase sensitivity problem. It also enables accurate core loss measurement for arbitrary waveform excitation without the requirement to fine-tune the cancellation component value.

All the aforementioned studies usually consider experimental test conditions performed on laboratory magnetic component prototypes, built or modified according to established measurement procedures. In principle, methods like [12][14] are applicable also for inductor loss measurement. However, for commercial preassembled shielded-core power inductors in real-world switching operating conditions, it could be more difficult to separate core (*ac* contribution only) and winding (*dc*+*ac* contributions) losses, mainly because the winding arrangement of commercial inductors can be quite irregular, and error sources cannot be prevented or attenuated [13]. Direct measurement of the *dc* and *ac* loss contributions for commercial power inductors is definitely more straightforward than the measurement of separate contributions for core and winding losses. It is worth noting that when high-frequency *ac* winding loss is negligible, the *ac* loss is due to core loss contribution only, whereas the *dc* loss is due to the *dc* winding resistance.

The inductor average total power loss P_{tot} is by definition the mean value of the instant power absorbed by the device over the switching period $T_s = 1/f_s$. The total power loss P_{tot} can be separated in two contributions in two different ways: winding and core losses (see Section II-A), or *dc* and *ac* losses (see Section II-B).

A. Winding and Core Losses

The total inductor power loss can be split as in (1):

$$P_{tot} = P_{wind} + P_{core} \tag{1}$$

Winding loss P_{wind} can be seen as the sum of *dc* and *ac* winding losses:

$$P_{wind,dc} = R_{dc} \cdot I_L^2 \tag{2}$$

$$P_{wind,ac} = R_{ac} \cdot I_{ac,rms}^2 \tag{3}$$

where R_{dc} is the *dc* winding resistance, R_{ac} is the *ac* winding resistance including high-frequency effects, and I_L and $I_{ac,rms}$ are the average and rms values of the *dc* and *ac* inductor current components, respectively. The *dc* loss can be easily evaluated from the *dc* winding resistance. The high-frequency winding loss can be predicted by using several methods [15]–[20], if the winding cross-sectional area and the layers distribution are known. Unfortunately, the manufacturers of commercial components do not disclose winding geometry data. The datasheets only provide the nominal value of R_{dc} resistance, obtained under *dc* test conditions. Therefore, since the exact R_{ac} resistance value is not available, the use of the R_{dc} resistance value to estimate the high-frequency *ac* winding loss can result in poor accuracy during the calculation of the total inductor loss.

Core loss P_{core} is investigated in several studies by considering the separation of hysteresis, eddy currents and excess loss contributions [21]–[23]. Unfortunately, the parameters of such models are not easy to obtain, since sophisticated experimental measurements are needed to evaluate separately the different loss terms. The Steinmetz Equation (SE), introduced in [24] and given in (4), represents *de facto* the empirical behavioral core loss formula mostly used in the SMPS design:

$$P_{core,SE} = C_m f_s^{\alpha} B_{ac}^{\beta} (A_e l_e) \tag{4}$$

where f_s is the excitation frequency, B_{ac} is the *ac* magnetic flux density magnitude, and A_e and l_e are the equivalent cross-sectional area and magnetic path length of the magnetic core. The coefficients C_m, α and β depend on core material, magnetic induction and switching frequency operating range, and are usually given in the datasheets of magnetic cores [25][26]. Since the peak-to-peak current ripple Δi_{Lpp} is easier to measure than the *ac* magnetic flux density B_{ac}, the SE can be reformulated as

a function of Δi_{Lpp}:

$$P_{core,SE} = K_1 f_s^X (K_2 \Delta i_{Lpp})^Y \quad (5)$$

where the coefficients K_1, K_2, X and Y depend on material and switching frequency range, and K_1 also depends on the core volume. Some power inductors manufacturers adopt the formulation given in (5) and provide relevant core loss coefficients [27]. More details on how to get coefficients $\{K_1, K_2, X, Y\}$ from coefficients $\{C_m, \alpha, \beta\}$ are provided in Appendix A.

Both models (4) and (5) are given for sinusoidal operating conditions. Several papers show how to extend the validity of the SE to nonsinusoidal conditions. In [28]–[32], enhanced versions of the SE have been proposed, namely the modified SE, the generalized SE, the *improved* Generalized Steinmetz Equation (*i*-GSE), the natural SE and the improved SE, valid for both sinusoidal and nonsinusoidal operating conditions and requiring no more parameters than the basic SE. In particular, Appendix A also describes how the *i*-GSE formula can be used for core loss calculation, given inductor voltage, duty-cycle, frequency and manufacturer's core loss coefficients.

However, all these formulations neglect the dependence of core loss on *dc* bias, thus yielding inaccurate core loss estimation in partial saturation conditions. Enhanced discussions on magnetic core loss models accounting for *dc* bias have been specifically proposed. In [33], Muhlethaler *et al.* have presented a study about the influence of premagnetization on magnetic material power loss. However, no analytical formulations have been given to model the SE parameters dependence on *dc* bias. In [34], Kosai *et al.* have proposed a correction to the SE for partial saturation operating conditions, based on a multiplicative exponential term depending on the ratio μ_0/μ. This ratio represents the saturation level of the core material, μ_0 being the magnetic permeability value at zero bias and μ being the effective magnetic permeability in partial saturation condition. However, neither μ_0 nor μ are easily measurable quantities for commercial magnetic devices. In [35], a core loss model has been proposed based on the use of a multiplicative bias factor as a function of the *dc* magnetic field H_{dc}. A quadratic term and a square root term of H_{dc} have been introduced to model the *dc* bias dependence for different magnetic materials. Finally, in [36], Sokalski *et al.* have suggested that the core loss function obeys the scaling law. Accordingly, a quite involved expression has been proposed, including the *dc* bias influence on core loss. Such formulation can be more accurate, yet too complicated for the SMPS designers. In fact, it involves a high number of model parameters not provided by magnetic components manufacturers, and requires magnetic quantities measurements, like the *ac* magnetic flux density B_{ac} and the *dc* magnetic field H_{dc}.

The main limitation of core loss models like [33]–[36] lies in the use of the magnetic quantities, which are not easy to measure for the commercial inductors operated in SMPS. In principle, some of such quantities can be estimated starting from the inductor voltage and current measurements, if the inductor winding turn number, the magnetic path length and cross-sectional area are known. Unfortunately, such data are not disclosed by the inductors manufacturers in their datasheets. For this reason, it is impossible to determine the parameters of the mentioned models by applying curve fitting techniques to the experimental core loss.

B. DC and AC Losses

The total inductor power loss can also be split as in (6):

$$P_{tot} = P_{dc} + P_{ac} \quad (6)$$

The *dc* loss P_{dc} depends on the *dc* components of inductor voltage V_L and current I_L, and can be evaluated as given in (7):

$$P_{dc} = V_L \cdot I_L = R_{dc} \cdot I_L^2 = P_{wind,dc} \quad (7)$$

which corresponds to (2). The *ac* loss P_{ac} depends on the *ac* components of the inductor voltage $v_{L,ac}(t)$ and current $i_{L,ac}(t)$, and is given by (8):

$$P_{ac} = f_s \int_0^{T_s} v_{L,ac}(t) \cdot i_{L,ac}(t)\, dt = P_{core} + P_{wind,ac} \quad (8)$$

where P_{core} is the magnetic core loss provided in (4) and (5), and $P_{wind,ac}$ is the *ac* winding loss contribution given in (3). This power loss separation (6) has the advantage of allowing the direct measurement of the two contributions (7) and (8), starting from the experimental waveforms of inductor voltage and current. In fact, the *dc* components of the measured waveforms provide the *dc* loss P_{dc} given in (7), while their *ac* components provide the *ac* loss P_{ac} given in (8).

Whatever experimental measurement technique is adopted to obtain $P_{ac} = P_{core} + P_{wind,ac}$, the measured values of the inductor *ac* loss can be used to determine an analytical behavioral model expressing the total *ac* loss as a function of the operating conditions imposed by the SMPS application. The new *ac* loss model proposed in this paper is based on this approach, and starts from the following assumptions:

1) the *ac* loss equation is expressed as a function of the switching frequency f_s, the average current I_L and the equivalent voltage $V_{eq} = D\ V_{L,on}$, where D is the converter duty-cycle and $V_{L,on}$ is the inductor voltage during the on-time interval D/f_s;
2) f_s and V_{eq} are the *input variables* of the *ac* loss equation, whereas I_L is an *input parameter* determining the value of the numerical coefficients of the loss equation.

It is worth noting that the inductor current ripple Δi_{Lpp} cannot be considered as an input of the *ac* loss equation if partial saturation conditions are considered. Indeed, the SMPS imposes f_s, I_L and V_{eq} to the inductor, which *responds* with certain current ripple Δi_{Lpp} and *ac* power loss P_{ac} depending on the saturation level. Therefore, different combinations of f_s, V_{eq} and I_L can result in the same current ripple magnitude, but with different levels of inductor saturation and *ac* power loss. The use of the equivalent voltage V_{eq} reflects the fact that the inductor *ac* power loss is only dependent on the volt-seconds applied to it, regardless of the SMPS topology.

III. GP-MOO Approach

In this Section, the GP-MOO approach adopted to identify the new *ac* loss model for FPIs is illustrated. The GP algorithm is an evolutionary algorithm where the population is composed

of models [7]. During its evolution, the GP algorithm transforms the current population of models into a new population of models, by applying classical genetic operations, such as selection, cross-over, mutation, elitism, etc. At the end of its evolution, the algorithm finds a model with the best-so-far fitness value. Only the main elements of the GP algorithm are summarized hereafter, as the GP is a known matter and it is out of the scope of the paper. The reader is also addressed to Appendix B for further details on the adopted GP algorithm.

For a given FPI, a set of m average current conditions I_{Lj} has been considered for the analysis, with $j = 1, ..., m$. For each current value, n couples of frequency and voltage conditions $\mathbf{x}_i = (f_{si}, V_{eqi})$ have been adopted, with $i = 1, ..., n$. For each of the $n \times m$ test conditions, a data vector has been created, including the test values $\mathbf{x}_i$ and the resulting *ac* power loss $y_{ij} = P_{ac,exp}(f_{si}, V_{eqi}, I_{Lj})$. The resulting *training* dataset $\mathcal{T}$ is shown in Table I. The GP algorithm was set to identify a global behavioral model (9):

$$P_{ac,bhv} = F\left(f_s, V_{eq}, \mathbf{p}(I_L)\right) \tag{9}$$

such that the value of the function F computed for each test condition of the training dataset $\mathcal{T}$ is as close as possible to the corresponding experimental value $y_{ij}, \forall i \in \{1, ..., n\}$ and $\forall j \in \{1, ..., m\}$. The structure of the behavioral power loss function F in (9) is the same for all the average current conditions, while the coefficients $\mathbf{p}$ are functions of I_L. To determine the values of coefficients $\mathbf{p}$, a Non-Linear Least Squares (NLLS) method has been applied to the n data vectors for each experimental current test condition I_{Lj}. Then, the interpolating function $\mathbf{p}(I_L)$ has been determined. The elements used by the GP algorithm to evaluate and select the *ac* loss models are as follows:

1) the *accuracy*, which can be estimated by means of the Root Mean Square Error (RMSE) between the experimental loss and the GP-predicted loss over the whole training dataset;
2) the *complexity*, which depends on the complexity of the elementary functions adopted in the model structure F. To quantify the global complexity of each GP model, the term $F_{complexity}$ has been introduced.

A more detailed description of the methods adopted to determine the coefficients $\mathbf{p}$ and of the *RMSE* and $F_{complexity}$ definitions is provided in Appendix B.

An elitist Nondominated Sorting Genetic Algorithm (NSGA-II) [37] has been used to discover the behavioral power loss model (9) offering a trade-off between the *RMSE* and the $F_{complexity}$ values over the whole training dataset. Such well-known MOO approach returns a Pareto front containing the non-dominated solutions present in the population, *i.e.* the solutions outperforming the other elements of the front in at least one objective, being worse in some other objectives. Herein, *RMSE* and $F_{complexity}$ have been considered as *objective functions* for minimization in the proposed MOO approach. Section IV discusses the GP-MOO approach adopted for the identification of the *ac* loss model for two FPIs (case studies #1 and #2). The resulting model is then tested and validated for other two FPIs, one with same magnetic material and core type (case study #3), and one with both different magnetic material and different core type (case study #4).

TABLE I
DATASET $\mathcal{T}$ OF THE GP ALGORITHM

	I_{L1}	I_{L2}	...	I_{Lm}
(f_{s1}, V_{eq1})	$(\mathbf{x}_1, y_{11})$	$(\mathbf{x}_1, y_{12})$	...	$(\mathbf{x}_1, y_{1m})$
(f_{s2}, V_{eq2})	$(\mathbf{x}_2, y_{21})$	$(\mathbf{x}_2, y_{22})$	...	$(\mathbf{x}_2, y_{2m})$
...	...	...	...	...
(f_{sn}, V_{eqn})	$(\mathbf{x}_n, y_{n1})$	$(\mathbf{x}_n, y_{n2})$	...	$(\mathbf{x}_n, y_{nm})$

TABLE II
INVESTIGATED INDUCTORS AND THEIR MAIN CHARACTERISTICS

Part Number	Dimensions $[mm^3]$	L $[\mu H]$	DCR $[m\Omega]$	$I_{sat}[A]$ 30% drop	$I_{rms}[A]$ 40°C rise
MSS1260-103	12x12x6	10	24	7.40	4.00
MSS1260-473	12x12x6	47	82	3.30	2.50
MSS1038-273	10.2x10x3.8	27	89	2.84	2.35
DO3316T-103	13.2x9.9x6.4	10	34	3.80	3.90

IV. GP-MOO-SIMULATED VERSUS EXPERIMENTAL RESULTS

The discussion is herein referred to power inductors with ferrite magnetic core. Inductors of different ferrite materials and core types have been considered for the investigation, with both shielded and unshielded magnetic cores, to obtain a generalized *ac* loss model valid for different FPIs.

Four inductors have been assumed for the investigation: the Coilcraft MSS1260-103 ($L_{nom} = 10\ \mu$H), MSS1260-473 ($L_{nom} = 47\ \mu$H) and MSS1038-273 ($L_{nom} = 27\ \mu$H), all assembled with shielded cores of same ferrite material, and the Coilcraft DO3316T-103 ($L_{nom} = 10\ \mu$H), assembled with an unshielded core of a different ferrite material. The main datasheet characteristics of these FPIs are listed in Table II.

Experimental data of the training dataset $\mathcal{T}$ have been collected by using the MADMIX system [38], shown in Fig. 1. Such automated measurement setup is able to measure the performance of power inductors under hard-switched conditions, reproducing exactly a real SMPS operation. In particular, the MADMIX allows to emulate the operation of an open-loop *dc–dc* converter: given the input voltage V_{IN}, the duty-cycle D, the switching frequency f_s and the output current I_{OUT}, the power inductor is subjected to an equivalent voltage $V_{eq} = V_{IN} \times D \times (1 - D)$ and a *dc* current $I_L = I_{OUT}$. Among all possible features, the MADMIX allows for imposing the desired SMPS-based operating conditions and makes high-speed measurements of the inductor voltage and current. Moreover, it can perform user-programmed tests over wide operating ranges and collect large series of measurement results, including *dc* and *ac* inductor power losses. Therefore, the training dataset for each inductor has been herein assembled by using the MADMIX system. Alternative acquisition methods for on-line FPIs characterization have been recently proposed, like in [39].

Each component has been tested in a wide range of inductor current, in order to cover both weak-saturation and roll-off region of the relative *L versus I* curve and guarantee power loss characterization also in partial saturation conditions. Maximum inductance derating of about 50% with respect to the nominal

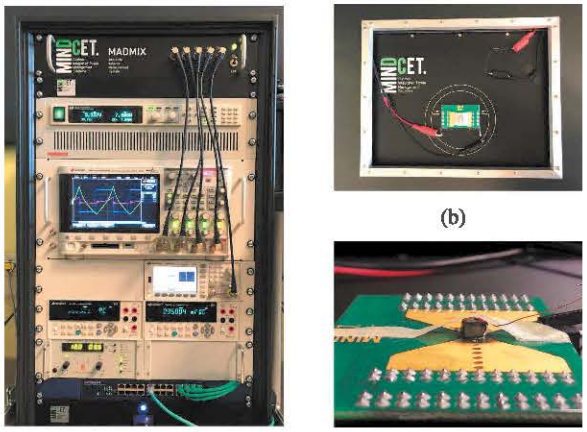

Fig. 1. MADMIX: (a) front panel, (b) top panel and (c) device under test.

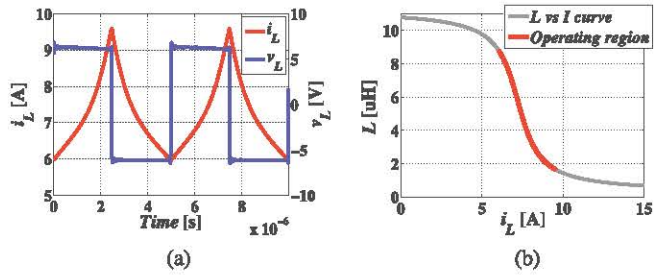

Fig. 2. MADMIX-based inductor waveforms: (a) voltage and current; (b) *L versus I* curve with relevant operating region.

inductance L_{nom} has been achieved for each inductor. As an example, voltage and current waveforms of a 10 μH Coilcraft MSS1260-103 inductor measured by the MADMIX are shown in Fig. 2(a). The datasheet *L versus I* curve of the inductor is shown in Fig. 2(b). The operating conditions adopted for the test are $V_{IN} = 12$ V, duty-cycle $D = 0.5$, switching frequency $f_s = 200$ kHz and average inductor current $I_L = 7.25$ A, involving the operation in the roll-off region (in Fig. 2(b), red portion of the curve). For this test example, the MADMIX measures an average inductance of 4.5 μH, a peak-to-peak current ripple of 3.34 A, a *dc* loss of 1.22 W (0.05% standard deviation), an *ac* loss of 175 mW (1.7% standard deviation), inductor and ambient temperatures of 71 °C and 26 °C, respectively.

The following sections discuss the application of the GP-MOO approach to the inductors of Table II.

A. Case Study #1: MSS1260-103 Inductor

To assemble the training dataset for the MSS1260-103 inductor, the operating conditions given in Table III have been fixed by means of the MADMIX system. All the possible combinations of such values have been tested, with $m = 13$ average current values and $n = 80$ operating conditions in terms of f_s and $V_{eq} = V_{IN} \times D \times (1 - D)$ for each current, resulting in a training dataset composed of $n \times m = 1040$ experimental data vectors. In particular, an inductance derating of 50% has been obtained at $I_L = 7.25$ A.

TABLE III
TRAINING SET OPERATING CONDITIONS FOR MSS1260-103 INDUCTOR

Quantity	Units	Values
f_s	kHz	[200, 300, 400, 500]
V_{IN}	V	[6, 8, 10, 12]
D	-	[0.2, 0.35, 0.5, 0.65, 0.8]
I_L	A	[3, 3.5, 4, 4.5, 5, 5.5, 5.75, 6, 6.25, 6.5, 6.75, 7, 7.25]

All the experimental measurements took about 35 h. Then, the GP-MOO approach has been applied to the composed training dataset: 30 independent GP algorithm runs have been executed to verify the repeatability of the obtained models, lasting about 15 h. Only the non-dominated Pareto-optimal solutions with the repeatability of at least 8 runs have been selected for a further comparison. Such solutions are shown as blue markers in Fig. 3. The two objective functions used during the GP-MOO routine – namely, the *RMSE* evaluated over the training dataset and the corresponding global complexity factor $F_{complexity}$ – are shown on the x and y axes, respectively. The solutions at the bottom-right side of this plot are characterized by very simple structures and very high errors with respect to experimental *ac* loss. Conversely, the solutions at the top-left side of the plot present the lowest errors and most complicated structures.

In order to select an optimal *ac* loss model among all the obtained Pareto-optimal solutions, several metrics have been considered to classify each model:

1) N_{run}: number of GP runs during which the algorithm has discovered the model (only models having $N_{run} \geq 8$ are shown in Fig. 3);
2) N_{gen}: average number of generations during which the model exists within the population (averaging done over N_{run});
3) μ_{err}: mean value of the percent error distribution of the model over the training dataset;
4) σ_{err}: standard deviation of the percent error distribution of the model over the training dataset;
5) err_{max}: maximum percent error of the model over the training dataset;
6) N_{mon}: average number of intervals over which the model coefficients change their monotonicity with respect to the *dc* current I_L.

Such metrics are shown in Fig. 3, next to the respective GP model expressions, from the more complicated ones (at the top of the list) to the simplest ones (at the bottom of the list). Among these solutions, the following model presents an optimal trade-off among all the six metrics

$$P_{ac,bhv} = p_0 exp\left(-p_1 f_s\right) V_{eq}^{p_2} + p_3 V_{eq}^2 \qquad (10)$$

where the coefficients $\{p_0, ..., p_3\}$ are the elements of the vector $\mathbf{p}(I_L)$ given in (9). The behavioral model (10) has a high repeatability ($N_{run} = 19$) and age ($N_{gen} = 186$) and shows excellent performances in terms of the percent fitting errors. It is characterized by a maximum percent error $err_{max} = 25\%$, with a mean percent error $\mu_{err} = 1\%$ and a standard deviation $\sigma_{err} = 5\%$. Only few models outperform the selected one in terms of the maximum percent error.

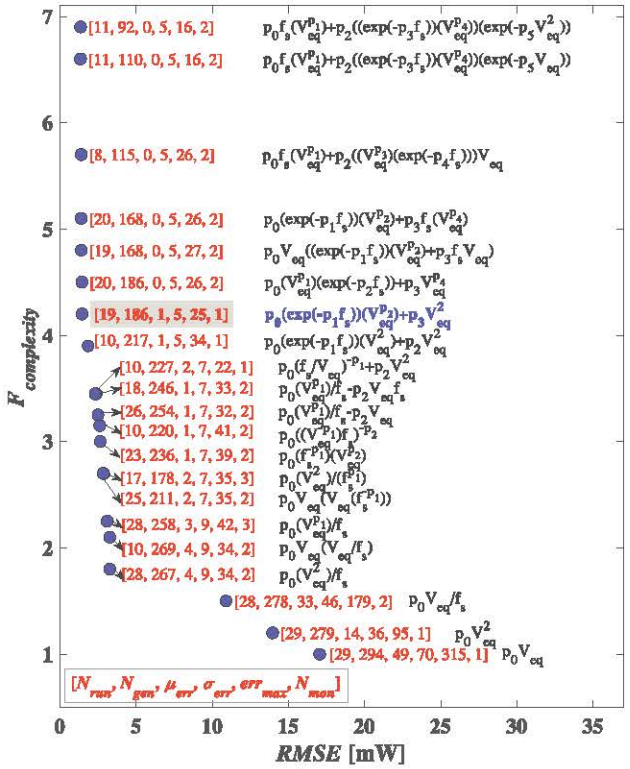

Fig. 3. Repeatable Pareto-optimal solutions for MSS1260-103 inductor.

In particular, the two models at the top of Fig. 3 have lower percent errors ($err_{max} = 16\%$), but a more complicated structure. Also the model described by the metrics values [10, 227, 2, 7, 22, 1] has a lower maximum percent error ($err_{max} = 22\%$), but higher mean percent error and standard deviation ($\mu_{err} = 2\%$, $\sigma_{err} = 7\%$). Moreover, the proposed *ac* loss model has monotonous coefficients with the *dc* current ($N_{mon} = 1$), thus resulting easier to be modeled with any curve fitting algorithm. The coefficients $\{p_0, \ldots, p_3\}$ of the model (10) are shown in Fig. 4 *versus* the average inductor current I_L, and can be modeled by means of the law (11):

$$\mathbf{p}(I_L) = \mathbf{a}_0 exp(\mathbf{a}_1 I_L) + \mathbf{a}_2 I_L + \mathbf{a}_3. \quad (11)$$

A NLLS algorithm has been used to determine the vector coefficients $\{\mathbf{a}_0, ..., \mathbf{a}_3\}$. The resulting fitting curves of the coefficients $\mathbf{p}$ are shown in Fig. 4, while the relative vector coefficients $\{\mathbf{a}_0, ..., \mathbf{a}_3\}$ are given in Table IV. Fig. 5(a)–(f) shows the relative percent errors between the predictions of behavioral model (10) and the experimental *ac* loss, for the four average current conditions $I_L = \{3, 5, 6, 7.25\}$ A, selected among the overall 13 current values included in the training dataset. The red markers correspond to the errors obtained by using the coefficients $\mathbf{p}$ of the proposed behavioral model, whereas the blue markers depict the errors obtained by using the NLLS fitting curves (11) of such coefficients. Each subplot shows the percent errors for 80 samples corresponding to different values of f_s and V_{eq}, at a fixed I_L value. For all markers, relative power loss error is within $\pm 15\%$ in weak-saturation region ($I_L \leq 6A$), and within $\pm 25\%$ in the roll-off region ($I_L > 6A$).

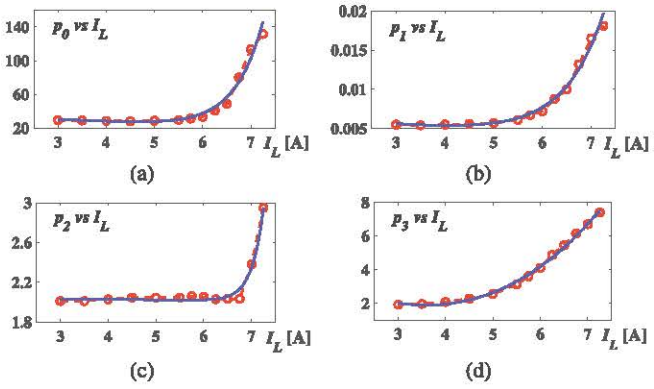

Fig. 4. Behavioral model coefficients (red) and the relative fitting curves (blue) for MSS1260-103.

TABLE IV
FITTING CURVES PARAMETERS OF THE BEHAVIORAL MODEL COEFFICIENTS FOR MSS1260-103

MSS1260-103 coefficients	$\mathbf{a}_0$	$\mathbf{a}_1$	$\mathbf{a}_2$	$\mathbf{a}_3$
p_0	5.76E-04	1.70E+00	-2.71E+00	3.86E+01
p_1	2.20E-06	1.23E+00	-4.16E-04	6.78E-03
p_2	9.65E-14	4.12E+00	-5.39E-03	2.05E+00
p_3	2.36E+01	1.36E-01	-5.23E+00	-1.78E+01

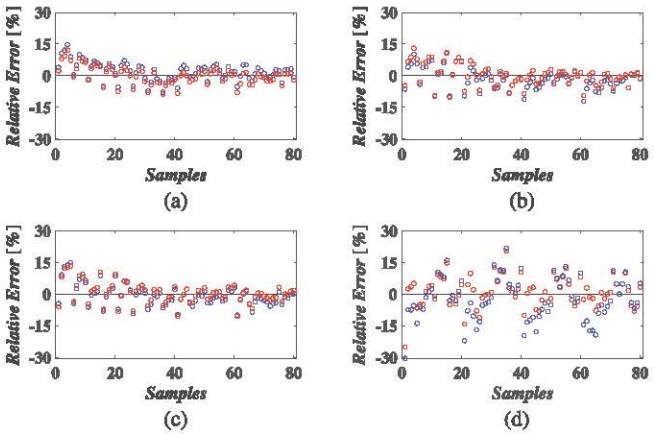

Fig. 5. Errors of $P_{ac,bhv}$ with the model coefficients (red) and the relative fitting curves (blue) for MSS1260-103: (a) $I_L = 3$A, (b) $I_L = 5$A, (c) $I_L = 6$A, (d) $I_L = 7.25$A.

For both weak-saturation and roll-off region, Fig. 6(a)–(b) compares the *ac* loss prediction errors of the proposed model $P_{ac,bhv}$ (red filled markers) with the errors of two benchmark models, evaluated as

- *benchmark model* $1 = ac$ winding loss + SE-based core loss (green filled markers);
- *benchmark model* $2 = ac$ winding loss + *i*-GSE-based core loss (green empty markers).

The *ac* winding loss has been evaluated as shown in (3), by using measured R_{dc} and $I_{ac,rms}$ values and taking into account the thermal effects on the winding resistance [3]. The SE-based core loss has been evaluated as shown in (5). In particular, the core loss coefficients $\{K_1, K_2, X, Y\}$ have been

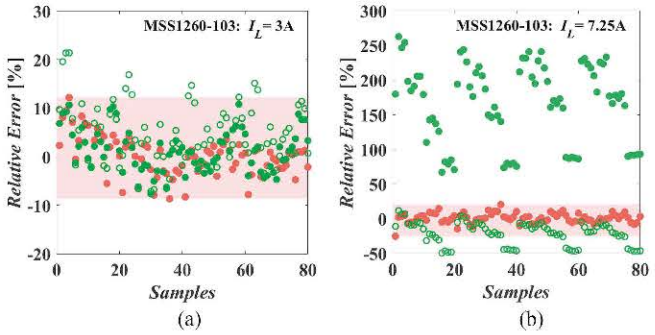

Fig. 6. Errors of $P_{ac,bhv}$ (red filled) *versus* benchmark model 1 (green filled) *versus* benchmark model 2 (green empty) for MSS1260-103: (a) in weak-saturation ($I_L = 3$A), (b) in roll-off ($I_L = 7.25$A).

estimated by means of the NLLS curve fitting of the benchmark model 1 applied to the experimental *ac* power loss in weak-saturation region. These coefficients have also been adopted to evaluate the *i*-GSE-based core loss, as discussed in detail in Appendix A.

The two benchmark models provide similar results in weak-saturation region (see Fig. 6(a)). On the contrary, in roll-off region the benchmark model 2 underestimates the *ac* power loss, whereas the benchmark model 1 hugely overestimates it (see Fig. 6(b)). Indeed, none of the two models include the dependence of core loss on *dc* bias. As discussed in [40], if Δi_{Lpp} value is maintained constant, the hysteresis loop area is expected to decrease with increasing current, as well as the resulting core loss. The benchmark model 1 does not include such core loss correction for *dc* bias and, as a result, overestimates the *ac* power loss. Conversely, if B_{ac} value is kept constant, the hysteresis loop area is expected to increase with the current, as well as the core loss. The benchmark model 2 does not include such *dc* bias dependence and underestimates the core loss. The results of Fig. 6 highlight that the proposed behavioral model (10) provides reliable *ac* loss estimation both in weak-saturation and in roll-off region.

B. Case Study #2: MSS1260-473 Inductor

In this second case study, the Coilcraft inductor MSS1260-473 of nominal inductance $L_{nom} = 47$ μH has been analyzed, having the same magnetic core of MSS1260-103, but different winding turn number. In order to reduce both measurements and execution times needed for the *ac* loss model identification, such inductor has been tested on the reduced set of 162 operating conditions given in Table V, including $m = 6$ average current values and $n = 27$ operating conditions in terms of f_s and V_{eq} for each current. In particular, an inductance derating of about 40% has been obtained at $I_L = 3.1$ A. The experimental measurements of such a reduced training dataset took about 6 h, whereas the 30 runs of the GP algorithm lasted about 2 h.

The GP-MOO algorithm has discovered the model (10) also for the MSS1260-473 inductor, even though the dimensions of the training dataset have been greatly reduced compared to the MSS1260-103 inductor (case study #1). Such model has a repeatability of 8 runs and persists in the population during

TABLE V
TRAINING SET OPERATING CONDITIONS FOR MSS1260-473 INDUCTOR

Quantity	Units	Values
f_s	kHz	[200, 300, 400]
V_{IN}	V	[12, 18, 24]
D	-	[0.3, 0.5, 0.7]
I_L	A	[1, 1.5, 2, 2.5, 2.8, 3.1]

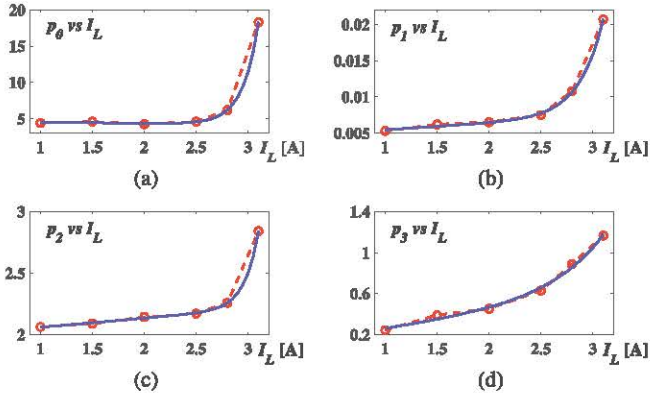

Fig. 7. Behavioral model coefficients (red) and the relative fitting curves (blue) for MSS1260-473.

TABLE VI
FITTING CURVES PARAMETERS OF THE BEHAVIORAL MODEL COEFFICIENTS FOR MSS1260-473

MSS1260-473 coefficients	a_0	a_1	a_2	a_3
p_0	1.63E-08	6.64E+00	-1.15E-01	4.58E+00
p_1	1.89E-08	4.35E+00	8.57E-04	4.62E-03
p_2	4.10E-11	7.57E+00	7.28E-02	1.99E+00
p_3	1.45E-03	1.95E+00	1.44E-01	1.07E-01

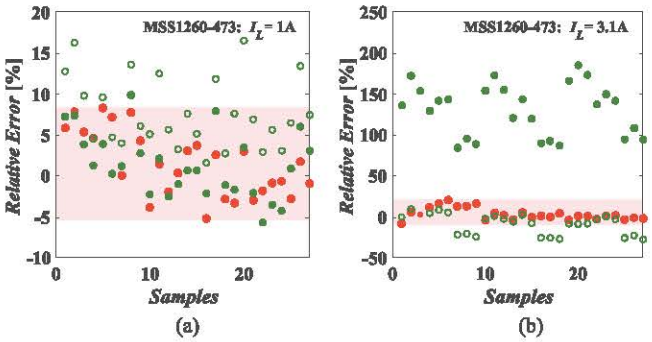

Fig. 8. Errors of $P_{ac,bhv}$ (red filled) *versus* benchmark model 1 (green filled) *versus* benchmark model 2 (green empty) for MSS1260-473: (a) in weak-saturation ($I_L = 1$A), (b) in roll-off ($I_L = 3.1$A).

148 generations, presents an average error $\mu_{err} = 2\%$, a standard deviation $\sigma_{err} = 5\%$ and a maximum error $err_{max} = 20\%$ over the training dataset, and its parameters are monotonic with the current I_L. The coefficients p of the model (10) for the MSS1260-473 inductor are shown in Fig. 7, together with their NLLS fitting curves. The values of the vector coefficients $\{a_0, ..., a_3\}$ of the fitting curves are given in Table VI.

Fig. 8(a)–(b) compares the *ac* loss prediction errors of the proposed model $P_{ac,bhv}$ with the errors of the two benchmark

models, for weak-saturation and roll-off region, respectively. Also for the MSS1260-473 inductor, the core loss coefficients $\{K_1, K_2, X, Y\}$ have been estimated by means of the NLLS curve fitting of the benchmark model 1 applied to the experimental *ac* power loss in weak-saturation region. As expected, the benchmark model 2 underestimates the *ac* loss in roll-off region, whereas the benchmark model 1 overestimates it.

C. Case Study #3: MSS1038-273 Inductor

The GP-MOO approach applied in the previous two case studies has led to the same *ac* power loss model for two inductors of the same family (same magnetic core). In this section, it is shown that the same model is valid for the devices of a different inductor family. In particular, the identification of the power loss model coefficients started directly from the model structure (10). In this case study, the inductor MSS1038-273 of nominal inductance $L_{nom} = 27$ μH has been considered, whose core has the same magnetic material but different size compared to the components of the MSS1260 family (see Table II). The 162 operating conditions given in Table VII have been considered, covering $m = 6$ average current values and $n = 27$ combinations of f_s and V_{eq} for each current. In particular, an inductance derating of about 50% has been obtained at $I_L = 2.9$ A.

The coefficients $\mathbf{p}$ of the model (10) are shown in Fig. 9, together with the NLLS fitting curves (11), whose parameters are given in Table VIII. The proposed behavioral model is characterized by a maximum percent error $err_{max} = 19\%$, with a mean percent error $\mu_{err} = 3\%$ and a standard deviation $\sigma_{err} = 6\%$ over the training dataset.

Fig. 10 (a)–(b) compares the *ac* loss prediction errors of the proposed model $P_{ac,bhv}$ with the errors of the two benchmark models, for weak-saturation and roll-off region, respectively. The $\{K_1, K_2, X, Y\}$ coefficients have been estimated as discussed for the previous case studies. As expected, the behavioral model (10) outperforms the two benchmark models, especially in partial saturation condition.

D. Case Study #4: DO3316T-103 Inductor

In this last case study, it is shown that the findings relevant to the identification of the *ac* power loss model have general validity. In fact, the *ac* power loss model has also been applied to inductors with different ferrite material, dimensions and type of the magnetic core. In particular, the Coilcraft inductor DO3316T-103 ($L_{nom} = 10$ μH) has been considered. This part is assembled with an unshielded core of different ferrite material and size with respect to the previously analyzed inductors (see Table II).

The *ac* loss formula has been kept unchanged for the Coilcraft DO3316T part: in fact, the identification of the power loss model coefficients started directly from the model structure (10). The 405 operating conditions given in Table IX have been considered, covering $m = 9$ average current values and $n = 45$ combinations of f_s and V_{eq} for each current. In particular, an inductance derating of about 50% has been obtained at $I_L = 4$ A.

TABLE VII
TRAINING SET OPERATING CONDITIONS FOR MSS1038-273 INDUCTOR

Quantity	Units	Values
f_s	kHz	[200, 300, 400]
V_{IN}	V	[8, 12, 16]
D	-	[0.3, 0.5, 0.7]
I_L	A	[0.9, 1.3, 1.7, 2.1, 2.5, 2.9]

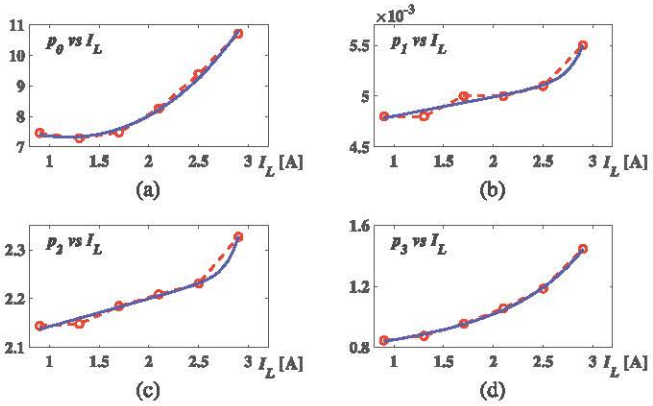

Fig. 9. Behavioral model coefficients (red) and the relative fitting curves (blue) for MSS1038-273.

TABLE VIII
FITTING CURVES PARAMETERS OF THE BEHAVIORAL MODEL COEFFICIENTS FOR MSS1038-273

MSS1038-273 coefficients	a_0	a_1	a_2	a_3
p_0	8.45E+00	3.77E-01	-4.96E+00	2.51E-14
p_1	1.75E-12	6.58E+00	1.88E-04	4.61E-03
p_2	4.30E-12	8.13E+00	5.72E-02	2.09E+00
p_3	4.81E-03	1.58E+00	7.85E-02	7.48E-01

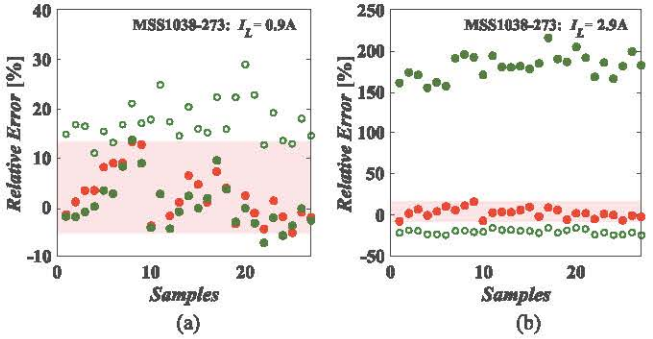

Fig. 10. Errors of $P_{ac,bhv}$ (red filled) *versus* benchmark model 1 (green filled) *versus* benchmark model 2 (green empty) for MSS1038-273: (a) in weak-saturation ($I_L = 0.9$A), (b) in roll-off ($I_L = 2.9$A).

The coefficients $\mathbf{p}$ of the model (10) are shown in Fig. 11, together with the NLLS fitting curves, whose parameters are given in Table X. The proposed behavioral model is characterized by a maximum percent error $err_{max} = 20\%$, with a mean percent error $\mu_{err} = 1\%$ and a standard deviation $\sigma_{err} = 3\%$ over the training dataset. Fig. 12(a)–(b) compares the *ac* loss prediction errors of the proposed model $P_{ac,bhv}$ with the errors of the two benchmark models, for weak-saturation and roll-off region,

TABLE IX
TRAINING SET OPERATING CONDITIONS FOR DO3316T-103 INDUCTOR

Quantity	Units	Values
f_s	kHz	[300, 400, 500]
V_{IN}	V	[8, 10, 12]
D	-	[0.2, 0.35, 0.5, 0.65, 0.8]
I_L	A	[2, 2.25, 2.5, 2.75, 3, 3.25, 3.5, 3.75, 4]

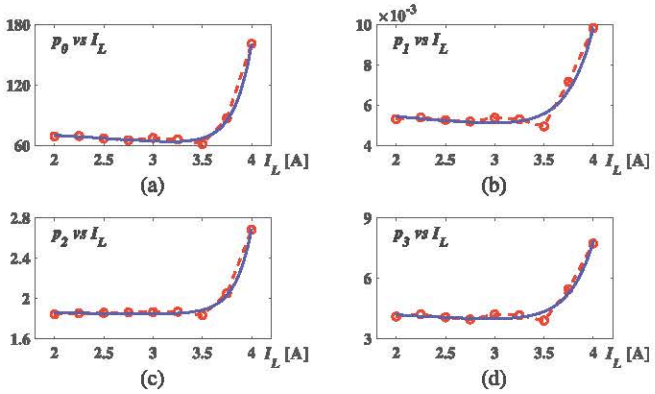

Fig. 11. Behavioral model coefficients (red) and the relative fitting curves (blue) for DO3316T-103.

TABLE X
FITTING CURVES PARAMETERS OF THE BEHAVIORAL MODEL COEFFICIENTS FOR DO3316T-103

DO3316T-103 coefficients	a_0	a_1	a_2	a_3
p_0	2.00E-08	5.59E+00	-6.21E+00	8.28E+01
p_1	1.61E-09	3.75E+00	-4.39E-04	6.32E-03
p_2	4.09E-11	5.94E+00	-1.04E-02	1.88E+00
p_3	4.33E-07	4.02E+00	-2.63E-01	4.72E+00

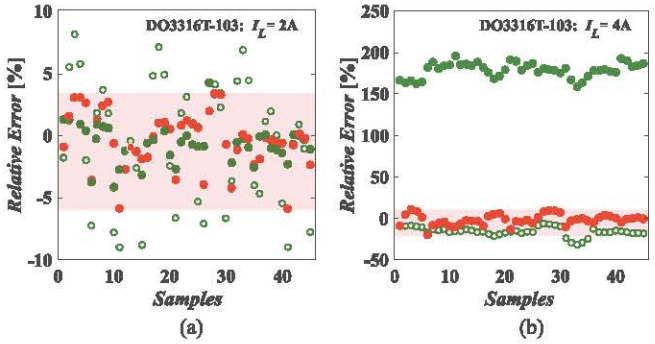

Fig. 12. Errors of $P_{ac,bhv}$ (red filled) *versus* benchmark model 1 (green filled) *versus* benchmark model 2 (green empty) for DO3316T-103: (a) in weak-saturation ($I_L = 2$A), (b) in roll-off ($I_L = 4$A).

respectively. The $\{K_1, K_2, X, Y\}$ coefficients have been estimated as discussed for the previous case studies. The behavioral model (10) outperforms the two benchmark models, especially in the partial saturation condition.

E. Model Discussion and Final Considerations

The behavioral model (10) is the sum of two terms: $p_0 exp\left(-p_1 f_s\right) V_{eq}^{p_2}$ and $p_3 V_{eq}^2$. The first term contains a power law dependence on the applied voltage V_{eq}, which reflects the dependence of P_{core} on the magnetic flux density magnitude B_{ac}, V_{eq} being proportional to B_{ac}. The second term contains a square-law dependence on the applied voltage V_{eq}, which reflects the dependence of $P_{wind,ac}$ on the peak-to-peak current ripple magnitude Δi_{Lpp}, V_{eq} being proportional to Δi_{Lpp}. Such result is in agreement with the expected loss trend, since the *ac* winding loss is proportional to the square of the rms *ac* current $I_{ac,rms}$, which can be well represented by the square of Δi_{Lpp} in case of a triangular or cusp-like inductor current waveform. The proposed model (10) also shows an exponential decay of the *ac* power loss with the increasing switching frequency, which can be explained as follows. For a fixed V_{eq} value, the peak-to-peak current ripple decreases while the frequency increases, result-ing in lower $I_{ac,rms}$ value. However, the winding resistance R_{ac} value increases at higher frequency, due to the skin and prox-imity effects. Thus, the *ac* winding loss $P_{wind,ac}$ can increase or decrease with the frequency, depending on the winding ar-rangement. As for the core loss P_{core}, a smaller peak-to-peak current ripple at higher frequencies involves a smaller B_{ac} mag-nitude and, consequently, a smaller area of the $B-H$ loop, which yields a loss reduction. However, the higher frequency involves that the $B-H$ loop is repeated more frequently, thus causing a consequent loss increase. As a result, the core loss could as increase as decrease with the frequency, depending on the inductor characteristics. For the components analyzed in this paper, the model (10) reveals that a frequency increase results in an *ac* power loss decrease.

Both the proposed *ac* loss model and the benchmark models used in this paper require experimental measurements data for model coefficients extraction. In particular, the GP-MOO algorithm adopted for the identification of model (10) also requires some extra computation time, when the behavioral models are generated for the first time. The amount of this additional time mainly depends on the experimental data used for models identification: the higher the number of the experimental test conditions, the greater the execution time required. However, the major benefit descending from the adoption of the GP-MOO algorithm is that it allows for the identification of a general loss model, valid for families of FPIs with different materials and/or core types and size, as proved by the four presented case studies. The identified model remains unchanged and always valid, in-dependently of the operating conditions the inductor is working in. Conversely, the suggested benchmark models are conserva-tive and can yield inaccurate core loss estimation, especially in partial saturation conditions. Once the *ac* loss model has been identified, only the execution time for the curve-fitting NLLS algorithm is needed to extract the model coefficient values. This time is comparable to that one needed for the extraction of any other benchmark models coefficients. Hence, the computation time of the GP-MOO algorithm execution is the unique extra time contribution for the proposed model.

F. Temperature Impact

Temperature is an important factor influencing the inductor power loss. The core loss density is sometimes modeled

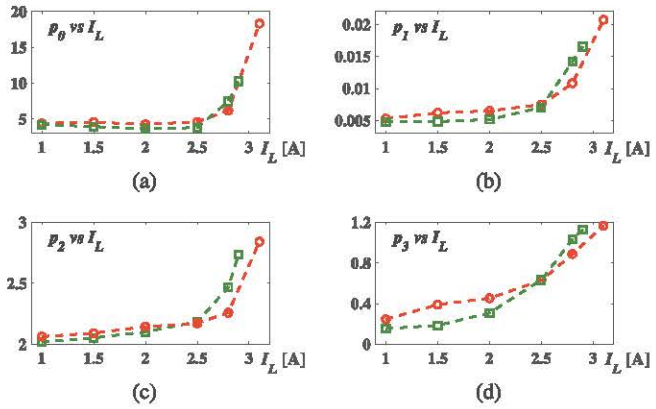

Fig. 13. Behavioral model coefficients at T_a=25 °C (red) and T_a=37 °C (green) for MSS1260-473.

as a polynomial function of temperature in magnetic cores datasheets [25], [26]. Unfortunately, few literature studies have investigated the dependence of the core loss on temperature. In [33], Muhlethaler *et al.* have introduced Steinmetz premagnetization graphs providing information about the dependence of the Steinmetz parameters on the *dc* bias for two different temperatures. Herein, the impact of the ambient temperature T_a on the coefficients of the proposed behavioral model (10) has been investigated for the MSS1260-473 inductor (case study #2). Experimental measurements of the *ac* power loss have been performed at T_a = 25 °C and T_a = 37 °C. The higher ambient temperature has been obtained by incapsulating the inductor into a heated chamber. The TDK B57550G502F 5kΩ±1% NTC thermistor has been used for the experimental measurements. For the two ambient temperature conditions, the coefficients of the behavioral model (10) have been identified by means of the NLLS technique, as shown in Fig. 13. It can be observed that, with the temperature increase, all the coefficients decrease in weak-saturation region (at low inductor currents $I_L < 2.5$ A) and increase in roll-off region (beyond 2.5 A inductor current). Indeed, while the ambient temperature increases, the inductance in weak-saturation region typically increases, thus resulting in the lower inductor current ripple and *ac* power loss. In roll-off region, instead, the inductance decreases with the temperature, thus resulting in higher current ripple and loss [41].

As future development of this research, more ambient temperature values will be tested to investigate the possibility to achieve a model with thermal trend of the coefficients $\mathbf{p}$.

Conclusions

In this paper, a new *ac* power loss model for FPIs in SMPS applications is proposed. The model has been obtained by means of the GP approach, in combination with the MOO technique, starting from experimental measurements of the component current, voltage and power loss in a wide range of SMPS operating conditions, including the FPI operation in partial saturation. The main difference of the proposed model with respect to prior art lies in the use of the applied voltage and switching frequency as variables of the power loss formula, while the *dc* current has been used as a parameter influencing the model coefficients to account for the impact of saturation. The results of the experimental tests presented in the paper prove that the proposed behavioral model provides quite reliable loss predictions, with a much higher accuracy compared to classical Steinmetz-based models, especially in partial saturation conditions. The proposed model is flexible and easy to apply to different families of FPIs, requiring only the use of a standard curve-fitting technique to identify the formula coefficients, based on the experimental data of the *ac* power loss.

Acknowledgments

The authors would like to thank Professor Antonio Della Cioppa, for providing insightful comments on genetic programming and evolutionary computation. The authors also thank Coilcraft, Inc., for providing inductors samples and relevant data.

Appendix A
Core Loss Models and Relevant Coefficients

A. Steinmetz Equation and Manufacturer's Coefficients

According to the SE, average core loss is given by (4). According to the manufacturer's formula, average core loss can be expressed as given in (5). In order to find the equivalence relations between the Steinmetz coefficients $\{C_m, \alpha, \beta\}$ and the manufacturer's coefficients $\{K_1, K_2, X, Y\}$, (12) and (13) can be used

$$v_L(t) = L[i_L(t)]\frac{di_L(t)}{dt} \tag{12}$$

$$v_L(t) = n\frac{d\Phi(t)}{dt} = nA_e\frac{dB(t)}{dt} \tag{13}$$

where n is the inductor winding turn number and Φ is the magnetic flux linkage of a single winding turn. From the equality of (12) and (13), it follows:

$$\int_0^{DT_s} L[i_L(t)]\frac{di_L(t)}{dt}dt = \int_0^{DT_s} nA_e\frac{dB(t)}{dt}dt$$

$$\Rightarrow \quad \int_{I_{L,min}}^{I_{L,max}} L(i_L)di_L = \int_{B_{min}}^{B_{max}} nA_e dB \tag{14}$$

where $I_{L,min}$ and $I_{L,max}$ are the minimum and maximum values of the inductor current waveform $i_L(t)$, whereas B_{min} and B_{max} are the minimum and maximum values of the magnetic flux density waveform $B(t)$. In weak saturation, $L(i_L) = L_{nom}$. This condition is normally adopted by manufacturers. Thus, (14) implies (15)

$$L_{nom}\Delta i_{Lpp} = 2nA_e B_{ac}$$

$$\Rightarrow \quad B_{ac} = \frac{L_{nom}}{2nA_e}\Delta i_{Lpp} = K_2\Delta i_{Lpp} \tag{15}$$

From (4), (5) and (15), the following equivalences can be eventually derived:

$$K_1 = C_m A_e l_e, \quad K_2 = \frac{L_{nom}}{2nA_e}, \quad X = \alpha, \quad Y = \beta \tag{16}$$

B. Improved Generalized Steinmetz Equation

According to the i-GSE [30], the average core loss is given as

$$P_{core,iGSE} = \frac{1}{T_s}\int_0^{T_s} k_i \left|\frac{dB}{dt}\right|^{\alpha} |\Delta B_{pp}|^{\beta-\alpha} (A_e l_e)\, dt \tag{17}$$

where $\Delta B_{pp} = 2B_{ac}$ and

$$k_i = \frac{C_m}{(2\pi)^{\alpha-1}\int_0^{2\pi} |\cos\theta|^{\alpha} 2^{\beta-\alpha} d\theta} \tag{18}$$

It can be shown that the integral term in (18) can be approximated as

$$\int_0^{2\pi} |\cos\theta|^{\alpha} d\theta \cong 4\left(0.2761 + \frac{1.7061}{\alpha + 1.354}\right) \tag{19}$$

The i-GSE can be reformulated in terms of the applied inductor voltage, duty-cycle, frequency and manufacturer's core loss coefficients $\{K_1, K_2, X, Y\}$. From (13), the following relations can be obtained:

$$\Delta B_{pp} = \int_0^{DT_s} \frac{v_L(t)}{nA_e} dt = \frac{V_{L,on}}{nA_e} DT_s = \frac{2K_2}{L_{nom}} V_{L,on} DT_s \tag{20}$$

$$\frac{dB}{dt} = \frac{v_L(t)}{nA_e} = \frac{2K_2}{L_{nom}} v_L(t) \tag{21}$$

where $V_{L,on}$ is the constant voltage applied to the inductor during the on-time interval. Hence, from (17), (20) and (21), we have

$$P_{core,iGSE} = \frac{k_v}{T_s}\int_0^{T_s} \left|\frac{2K_2 v_L(t)}{L_{nom}}\right|^{X} \left|\frac{2K_2 V_{L,on} DT_s}{L_{nom}}\right|^{Y-X} dt \tag{22}$$

where

$$k_v = k_i (A_e l_e) = \frac{K_1}{(2\pi)^{X-1}\int_0^{2\pi} |\cos\theta|^{X} 2^{Y-X} d\theta}. \tag{23}$$

By means of algebra, we obtain

$$P_{core,iGSE} = f_s k_v \left[\frac{2K_2}{L_{nom}}\right]^{Y} [V_{L,on} DT_s]^{Y-X} \cdot \ldots$$

$$\cdot \int_0^{T_s} |v_L(t)|^{X} dt = k_v \left[\frac{2K_2}{L_{nom}}\right]^{Y} \left[\frac{V_{L,on} D}{f_s}\right]^{Y-X} \cdot \ldots \tag{24}$$

$$\cdot\ D\,|V_{L,on}|^{X} + (1-D)\,|V_{L,off}|^{X}$$

where $V_{L,off}$ is the constant voltages applied to the inductor during the off-time interval of the converter. In such reformulation, the i-GSE jointly depends on the applied inductor voltages, duty-cycle and frequency, and manufacturer's core loss coefficients $\{K_1, K_2, X, Y\}$.

APPENDIX B
GP ALGORITHM SPECIFICATIONS

The GP models are generally represented by means of tree structures. To construct such trees, the GP algorithm makes use of a given set of elementary functions, constant coefficients and independent variables or model inputs. By definition, the group of independent variables and constant coefficients composes the *terminal set*, and the group of elementary functions represent the *non-terminal set* the GP algorithm works with. Both terminal and non-terminal sets adopted in this paper are shown in Table XI. The main GP algorithm settings and parameters are given in Table XII.

TABLE XI
NON-TERMINAL AND TERMINAL SETS

#inputs	Non-terminal	Description	Complexity
2	sum	$f+g$	1
2	multiplication	$f \cdot g$	1
2	power	f^g	1.5
2	division	f/g	1.5
1	logarithm	$\log(f)$	1.5
1	natural exp.	$\exp(f)$	1.5
1	power	f^{α}	1.5
1	exponential	α^f	1.5
1	square root	$\sqrt{f}$	1.5
1	hyperbolic tangent	$\tanh(f)$	1.5
1	inverse tangent	$\tan^{-1}(f)$	1.5
1	reciprocal	$1/f$	1.5

#inputs	Terminal	Description	Complexity
0	input	$\mathbf{x} = \{f_s, V_{eq}\}$	0.6 (for multiplication) 1.0 (for other operations)
0	coefficient	p	1

TABLE XII
GP ALGORITHM SETTINGS AND PARAMETERS [43]

Description	Value
Population size	500
Generation number	300
Maximum tree size	50 nodes
Selection operator	binary tournament
Cross-over operator	subtree cross-over
Mutation operator	subtree & node mutation
Cross-over probability	0.80
Subtree mutation probability	0.18
Node mutation probability	0.02

A. Complexity Evaluation

In the literature, several methods have been proposed to estimate the global complexity of the GP models [42]. In this paper, the elements of the terminal and non-terminal sets have been assigned different complexity factors, and on their basis the global complexity of each constructed GP model has been estimated. Each element of the terminal set has been assigned a complexity factor equal or lower than one, whereas each element of the non-terminal set has been assigned a complexity factor equal or greater than one. The input variables $\mathbf{x} = \{f_s, V_{eq}\}$ have been assigned a unit complexity factor, except for the multiplication operations between such variables, for which a complexity factor of 0.6 has been attributed to each input, in order to prevent an excessive penalization of quadratic and cubic terms, such as f_s^2, V_{eq}^3, $f_s \cdot V_{eq}$, etc.

To quantify the global complexity of each GP model, the term $F_{complexity}$ has been introduced, based on the complexity values given in Table XI and calculated in the following way:

- if a function (non-terminal element) is the argument of another function, the complexity factors of the two functions are multiplied;

- if two functions are multiplied or summed, their complexity factors are summed and subsequently multiplied by the complexity factor of a sum or a product, respectively.

In the first case, a vertical development of the models (*i.e.*, involved functions of functions) is prevented, especially for the functions with great complexity. In the second case, a horizontal development of the models is prevented, *i.e.*, models composed of many simple functions multiplied or summed among them, when a single more complicated function (*e.g.*, exponential or power function) could be sufficient to model the quantity of interest. For instance, using the complexity factors from Table XI, the global complexity $F_{complexity}$ of the model $P_{ac} = p_0 exp\left(-p_1 f_s\right) V_{eq}^{p_2} + p_3 V_{eq}^2$ given in (10) can be calculated as follows: $F_{complexity} = 1 \cdot (1.5 + 1.5) + 1 \cdot (0.6 + 0.6) = 4.2$.

B. Accuracy Evaluation

To determine the coefficients $\mathbf{p}$ of the GP-based model (9) for each average inductor current I_{Lj} $(j = 1, ..., m)$, a NLLS method has been applied to the n experimental data vectors relative to I_{Lj}. In particular, a Levenberg–Marquardt least square optimization method has been adopted [44]. Such algorithm starts from the model structure provided by the GP algorithm and finds the best coefficients values $\mathbf{p}$ for each average current. The χ-squared error criterion has been applied to the experimental loss y_{ij} and the GP-predicted loss $F\left(f_{si}, V_{eqi}, \mathbf{p}\left(I_{Lj}\right)\right)$, as follows:

$$\chi_j^2 = \frac{1}{n} \sum_{i=1}^{n} \left\{ F\left(f_{si}, V_{eqi}, \mathbf{p}\left(I_{Lj}\right)\right) - y_{ij} \right\}^2 \tag{25}$$

The values of coefficients $\mathbf{p}$ for each average current I_{Lj} have been determined by minimizing χ_j^2. To estimate the global accuracy of the GP-based model over the whole training dataset, the *RMSE* between the experimental and the GP-predicted losses has been estimated by means of (26):

$$RMSE = \sqrt{\frac{1}{m} \sum_{j=1}^{m} \chi_j^2} \tag{26}$$

REFERENCES

[1] L. Milner and G. A. Rincon-Mora, "Small saturating inductors for more compact switching power supplies," *IEEJ Trans. Electric. Electron. Eng.*, vol. 7, no. 1, pp. 69–73, Jan. 2012.

[2] "Power inductors and peak current handling capability," Renco Electronics, Rockledge, FL, USA, 2016.

[3] G. Di Capua, N. Femia, and K. Stoyka, "Switching power supplies with ferrite inductors in sustainable saturation operation," *Int. J. Elect. Power Energy Syst.*, vol. 93, no. Supplement C, pp. 494–505, Dec. 2017.

[4] C. Wilhelm, D. Kranzer, and B. Burger, "Development of a highly compact and efficient solar inverter with silicon carbide transistors," in *Proc. 6th Int. Conf. Integr. Power Electron. Syst.*, Mar. 2010, pp. 1–6.

[5] A. Stadler, T. Stolzke, and C. Gulden, "Nonlinear power inductors for large current crest factors," in *Proc. Eur. Power Convers. Intell. Motion Conf.*, May 2012, pp. 1548–1553.

[6] G. Di Capua and N. Femia, "A novel method to predict the real operation of ferrite inductors with moderate saturation in switching power supply applications," *IEEE Trans. Power Electron.*, vol. 31, no. 3, pp. 2456–2464, Mar. 2016.

[7] J. R. Koza, *Genetic Programming: On the Programming of Computers by Means of Natural Selection*. Cambridge, MA, USA: MIT Press, 1992.

[8] V. J. Thottuvelil, T. G. Wilson, and H. A. Owen, "High-frequency measurement techniques for magnetic cores," *IEEE Trans. Power Electron.*, vol. 5, no. 1, pp. 41–53, Jan. 1990.

[9] A. Brockmeyer, "Experimental evaluation of the influence of dc-premagnetization on the properties of power electronic ferrites," in *Proc. 11th Annu. IEEE Appl. Power Electron. Conf. Expo.*, Mar. 1996, pp. 454–460.

[10] M. Mu, Y. Su, Q. Li, and F. C. Lee, "Magnetic characterization of low temperature co-fired ceramic (LTCC) ferrite materials for high frequency power converters," in *Proc. IEEE Energy Convers. Congr. Expo.*, Sep. 2011, pp. 2133–2138.

[11] Y. Han, G. Cheung, A. Li, C. R. Sullivan, and D. J. Perreault, "Evaluation of magnetic materials for very high frequency power applications," *IEEE Trans. Power Electron.*, vol. 27, no. 1, pp. 425–435, Jan. 2012.

[12] M. Mu, Q. Li, D. J. Gilham, F. C. Lee, and K. D. T. Ngo, "New core loss measurement method for high-frequency magnetic materials," *IEEE Trans. Power Electron.*, vol. 29, no. 8, pp. 4374–4381, Aug. 2014.

[13] M. Mu, F. C. Lee, Q. Li, D. Gilham, and K. D. T. Ngo, "A high frequency core loss measurement method for arbitrary excitations," in *Proc. 26th Annu. IEEE Appl. Power Electron. Conf. Expo.*, Mar. 2011, pp. 157–162.

[14] D. Hou, M. Mu, F. C. Lee, and Q. Li, "New high-frequency core loss measurement method with partial cancellation concept," *IEEE Trans. Power Electron.*, vol. 32, no. 4, pp. 2987–2994, Apr. 2017.

[15] P. L. Dowell, "Effects of eddy currents in transformer windings," *Proc. Inst. Elect. Eng.*, vol. 113, no. 8, pp. 1387–1394, Aug. 1966.

[16] J. P. Vandelac and P. D. Ziogas, "A novel approach for minimizing high-frequency transformer copper losses," *IEEE Trans. Power Electron.*, vol. 3, no. 3, pp. 266–277, Jul. 1988.

[17] J. A. Ferreira, "Improved analytical modeling of conductive losses in magnetic components," *IEEE Trans. Power Electron.*, vol. 9, no. 1, pp. 127–131, Jan. 1994.

[18] C. R. Sullivan, "Computationally efficient winding loss calculation with multiple windings, arbitrary waveforms, and two-dimensional or three-dimensional field geometry," *IEEE Trans. Power Electron.*, vol. 16, no. 1, pp. 142–150, Jan. 2001.

[19] J. Hu and C. R. Sullivan, "AC resistance of planar power inductors and the quasidistributed gap technique," *IEEE Trans. Power Electron.*, vol. 16, no. 4, pp. 558–567, Jul. 2001.

[20] A. Reatti and M. K. Kazimierczuk, "Comparison of various methods for calculating the *ac* resistance of inductors," *IEEE Trans. Mag.*, vol. 38, no. 3, pp. 1512–1518, May 2002.

[21] M. Sippola and R. E. Sepponen, "Accurate prediction of high-frequency power-transformer losses and temperature rise," *IEEE Trans. Power Electron.*, vol. 17, no. 5, pp. 835–847, Sep. 2002.

[22] W. A. Roshen, "A practical, accurate and very general core loss model for nonsinusoidal waveforms," *IEEE Trans. Power Electron.*, vol. 22, no. 1, pp. 30–40, Jan. 2007.

[23] T. Hatakeyama and K. Onda, "Core loss estimation of various materials magnetized with the symmetrical/asymmetrical rectangular voltage," *IEEE Trans. Power Electron.*, vol. 29, no. 12, pp. 6628–6635, Dec. 2014.

[24] C. P. Steinmetz, "On the law of hysteresis," *Proc. IEEE*, vol. 72, no. 2, pp. 197–221, Feb. 1984.

[25] "Curve fit equations for ferrite materials," Magnetics, Inc., 1999.

[26] "Design of planar power transformers," Ferroxcube, 1997.

[27] P1172 Datasheet, Pulse Electronics, 2007.

[28] J. Reinert, A. Brockmeyer, and R. W. A. A. De Doncker, "Calculation of losses in ferro- and ferrimagnetic materials based on the modified Steinmetz equation," *IEEE Trans. Ind. Appl.*, vol. 37, no. 4, pp. 1055–1061, Jul. 2001.

[29] J. Li, T. Abdallah, and C. R. Sullivan, "Improved calculation of core loss with nonsinusoidal waveforms," in *Proc. IEEE 36th IAS Annu. Meet. Ind. Appl. Conf.*, Sep. 2001, pp. 2203–2210, vol. 4.

[30] K. Venkatachalam, C. R. Sullivan, T. Abdallah, and H. Tacca, "Accurate prediction of ferrite core loss with nonsinusoidal waveforms using only Steinmetz parameters," in *Proc. IEEE Workshop Comput. Power Electron.*, Jun. 2002, pp. 36–41.

[31] A. Van den Bossche, V. C. Vaichev, and G. B. Georgiev, "Measurement and loss model of ferrites with non-sinusoidal waveforms," in *Proc. IEEE 35th Annu. Power Electron. Spec. Conf.*, Jun. 2004, pp. 4814–4818, vol. 6.

[32] S. Barg, K. Ammous, M. Hanen, and A. Ammous, "An improved empirical formulation for magnetic core losses estimation under non-sinusoidal induction," *IEEE Trans. Power Electron.*, vol. 32, no. 3, pp. 2146–2154, Mar. 2017.

[33] J. W. Kolar, J. Muhlethaler, J. Biela, and A. Ecklebe, "Core losses under the *dc* bias condition based on Steinmetz parameters," *IEEE Trans. Power Electron.*, vol. 27, no. 2, pp. 953–963, Feb. 2012.

[34] H. Kosai, Z. Turgut, and J. Scofield, "Experimental investigation of dc-bias related core losses in a boost inductor," *IEEE Trans. Mag.*, vol. 49, no. 7, pp. 4168–4171, Jul. 2013.
[35] M. Mu, "High frequency magnetic core loss study," Ph.D. dissertation, Dept. Elect. Eng., Virginia Tech., Blacksburg, VA, USA, 2013.
[36] A. Ruszczyk, K. Sokalski, and J. Szczyglows, "Scaling in modeling of core losses in soft magnetic materials exposed to nonsinusoidal flux waveforms and DC bias," in *Proc. 21st Soft Mag. Mater. Conf.*, Aug. 2013.
[37] K. Deb, A. Pratap, S. Agarwal, and T. Meyarivan, "A fast and elitist multiobjective genetic algorithm: NSGA-II," *IEEE Trans. Evol. Comput.*, vol. 6, no. 2, pp. 182–197, Apr. 2002.
[38] M. Wens and J. Thone, "MADMIX: The standard for measuring SMPS inductors," *Bodo's Power Syst.*, pp. 52–54, Apr. 2015.
[39] M. Lodi, A. Oliveri, and M. Storace, "Low-cost acquisition method for on-line inductor characterization in switched power converters," in *Proc.14th Int. Conf. Synthesis, Model., Anal. Simul. Methods Appl. Circuit Design*, Jun. 2007.
[40] K. Terashima, K. Wada, T. Shimizu, T. Nakazawa, K. Ishii, and Y. Hayashi, "Evaluation of the iron loss of an inductor based on dynamic minor characteristics," in *Proc. Eur. Conf. Power Electron. Appl.*, Sep. 2007, pp. 1–8.
[41] *Power Choke Coils for Automotive Applications*, Panasonic Industry Europe. [Online]. Available: https://eu.industrial.panasonic.com/node/2539/power-choke-coils-automotive-applications
[42] J. Ni and P. Rockett, "Tikhonov regularization as a complexity measure in multiobjective genetic programming," *IEEE Trans. Evol. Comput.*, vol. 19, no. 2, pp. 157–166, Apr. 2015.
[43] W. B. Langdon, R. Poli, N. F. McPhee, and J. R. Koza, *Genetic Programming: An Introduction and Tutorial, With a Survey of Techniques and Applications*. Berlin, Germany: Springer, 2008, pp. 927–1028. [Online]. Available: https://doi.org/10.1007/978-3-540-78293-3_22
[44] W. H. Press, S. A. Teukolsky, W. T. Vetterling, and B. P. Flannery, *Numerical Recipes in C: The Art of Scientific Computing*. 2nd ed. New York, NY, USA: Cambridge Univ. Press, 1992.

Kateryna Stoyka was born in Khust, Ukraine, in 1989. She received the B.Sc. and M.Sc. degrees (Hons.) in electronic engineering from the University of Salerno, Fisciano, Italy, in 2011 and 2015, respectively, where she is currently working toward the Ph.D. degree in computing and information engineering.

Her main research interests include analysis and design of switching mode power supplies, power magnetics, numerical techniques for identification and optimization of behavioral models of power devices and systems.

Giulia Di Capua (S'06–M'13) received the B.Sc. and M.Sc. degrees (Hons.) in electronic engineering, and the Ph.D. degree in information engineering from the University of Salerno, Fisciano, Italy, in 2006, 2009, and 2013, respectively.

She is currently an Assistant Professor with the Department of Information and Electrical Engineering and Applied Mathematics, University of Salerno, Fisciano, Italy. Her research interests include switching mode power supplies optimization, magnetic components design and wireless power transfer.

Dr. Di Capua was the General Chair of the 2017 International Conference on Synthesis, Modeling, Analysis and Simulation Methods and Applications to Circuit Design. She is member of the Power and Energy Circuits and Systems Technical Committee of the IEEE CAS Society.

Nicola Femia (M'94–SM'13) received the Laurea degree (Hons.) in industrial technologies engineering from the University of Salerno, Fisciano, Italy, in 1988.

He was a Visiting Professor with the Department of Electrical Engineering, Stanford University, Stanford, CA, USA, where he taught power electronics control and energy aware design in the Electrical Engineering Enhanced Master Program. He is currently a Full Professor with the University of Salerno, where he teaches power electronics and energetic intelligence in the Electronic Engineering and Computer Engineering Master Programs and leads the Power Electronics and Renewable Sources Laboratory. He has coauthored more than 190 scientific papers published in international journals and proceedings of international conferences, and six patents. Over the past 25 years, he has promoted and directed worldwide university and industry research activities and education programs on power electronics, photovoltaic systems and power design.

Prof. Femia was an Associate Editor of the IEEE TRANSACTIONS ON POWER ELECTRONICS from 1995 to 2003.